Research Square

Preprints are preliminary reports that have not undergone peer review.
They should not be considered conclusive, used to inform clinical practice,
or referenced by the media as validated information.

Introducing field evaporation energy loss spectroscopy

Loïc ROUSSEAU (loic.rousseau6@univ-rouen.fr)
University of Rouen https://orcid.org/0000-0003-3659-9070

Antoine Normand
University of Rouen

Felipe F. Morgado
Max-Planck Institut für Eisenforschung GmbH

Hanne S. Soreide
Norwegian University of Science and Technology

Leigh Stephenson
Max-Planck-Institut für Eisenforschung GmbH, Germany https://orcid.org/0000-0002-7852-2509

Constantinos Hatzoglou
Norwegian University of Science and Technology

Gérald Da Costa
University of Rouen

Kambiz Tehrani
Esigelec

Christoph Freysoldt
Max-Planck-Institut für Eisenforschung GmbH https://orcid.org/0000-0002-7896-3478

Baptiste Gault
Max Planck Institute for Iron Research https://orcid.org/0000-0002-4934-0458

François Vurpillot
Normandie University https://orcid.org/0000-0002-6834-3507

Article

Keywords: Atom Probe Tomography, Energy barrier, Field Evaporation, Field Evaporation Energy Loss Spectroscopy, Time-of-Flight Mass Spectrometry

Posted Date: June 16th, 2022

DOI: https://doi.org/10.21203/rs.3.rs-1652464/v1

License: This work is licensed under a Creative Commons Attribution 4.0 International License.
Read Full License

Introducing field evaporation energy loss spectroscopy

Loïc Rousseau[1*], Antoine Normand[1], Felipe F. Morgado[2], Hanne-Sofie Marie Scisly Søreide[3], Leigh T. Stephenson[2], Constantinos Hatzoglou[3], Gérald Da Costa[1], Kambiz Tehrani[4], Christoph Freysoldt[2], Baptiste Gault[2,5] and François Vurpillot[1]

[1*]Groupe de Physique des Matériaux, UMR6634 CNRS, Université de Rouen, Saint-Etienne du Rouvray, 76800, Normandie, France.
[2]Max-Planck Institut für Eisenforschung GmbH, Organization, Düsseldorf, D-40237, State, Germany.
[3]Department of Materials Science and Engineering, Norwegian University of Science and Technology, Trondheim, 7491, State, Norway.
[4]ESIGELEC, Saint-Etienne du Rouvray, 76800 , Normandie, France.
[5]Department of Materials,Royal School of Mines, Imperial College London, London, SW 2AZ , United Kingdom, France.

*Corresponding author(s). E-mail(s): loic.rousseau6@univ-rouen.fr;
Contributing authors: francois.vurpillot@univ-rouen.fr;

Abstract

Identifying the chemical and bonding state of all atoms in a material in three-dimensions remains an unresolved issue. Here, we demonstrate that this information was always intrinsically present within atom probe tomography experimental data, but until now it was overlooked or consciously suppressed. Using an analytical model and robust simulations, we show that the mass peak shape contains information on the ion's energy loss related to how the atom was bound

to the surface, and its neighbourhood. We introduce a complete data processing approach, termed field evaporation energy loss spectroscopy (FEELS), that retrieves and maps variations of the chemical state in 3D with nanometric resolution. We showcase the application of FEELS by analyzing microstructural features and defects in an array of metallic materials. FEELS can be applied on any atom probe data set to more profoundly analyse a material's characteristics.

Keywords: Atom Probe Tomography, Energy barrier, Field Evaporation, Field Evaporation Energy Loss Spectroscopy, Time-of-Flight Mass Spectrometry

1 Introduction

There is a gap in the cornucopia of microscopy and microanalysis techniques for a three-dimensional technique able to access the bonding state of atoms with a resolution better than a nanometer. A possible approach to achieve this is to quantify the energetic bindings of an atom to its neighbor by exploiting the field evaporation phenomena that underpin atom probe tomography (APT). APT uses an intense electric field generated at the apex of a sharp needle-shaped specimen to locally break atomic bonds between surface atoms, allowing a precise control of their removal [1]. The atoms constituting the material itself are thus ionized and projected by the divergent electrostatic field, and collected by a position- and time-sensitive single particle detector. Post-processing algorithms are used to assign an elemental nature to each ion using time-of-flight mass spectrometry (TOF-MS) and to reconstruct a 3D near-atomic scale map of the field evaporated volume. [2, 3].

APT allows compositional analysis of individual microstructural features with a high sensitivity [4]. However, strong differences in the surface atoms' binding strength change the electric field required for their field evaporation. Hence, it alters the sequences [1] in which the atoms are removed and mesoscale changes in the specimen's shape that lead to trajectory aberrations [5–8], reconstruction artefacts [9], and species-specific losses due to preferential field evaporation of a species [10–12]. Those effects combine to limit the ultimate spatial resolution of the technique [7, 13–18] and to prevent the direct imaging of the complete crystalline lattice [14, 19–21]. Studies [22–24] have proposed the use of multiple field evaporation events to infer bonding mechanisms in thermoelectric and phase change materials, but APT cannot readily inform on the energetics of atomic bonds inside the material itself, merely at its surface under an intense electric field. After data mining, the spatial resolution at the near-atomic scale is also lost and the relationship between the chemical state of an atom and its field evaporation behavior cannot be readily determined.

Correlative workflows enable to combine APT's compositional measurement with structural and chemical analyses by using (scanning) transmission electron microscopy ((S)TEM). (S)TEM can retrieve grain orientations, the

structure of interfaces or complex phases, structural defects such as interfaces, dislocations, slip bands or stacking faults [25], as well as direct probing of physical properties [26, 27]. Spectroscopy of the energy lost by the electrons exiting the imaged specimen (electron energy loss spectroscopy - EELS) provides chemical information in a two-dimensional projection through the specimen's thickness, with a resolution approaching single-atomic columns. Contrary to APT, EELS provides direct information on inter-atomic bonding or on local modes of electronic or phonon vibration [28, 29]. Nevertheless, the chemical sensitivity of (S)TEM-based methods is only around $1at.\%$ [29], and the projected image makes the precise analysis of small microstructural features embedded in a matrix challenging.

Here, we showcase how APT can readily bring insights into the binding of surface atoms by reprocessing existing dataset. From the physics of field evaporation, we introduce an energetic parameter, which has a direct link to the field evaporation energy barrier and encodes information on the local surface atomic neighborhoods that can be mapped in 3D at the nanometer scale, leading to a new approach termed field evaporation energy loss spectroscopy (FEELS). We report on the application of FEELS to pure metals and metallic alloys, including at structural defects to demonstrate that our approach provides a three-dimensions mapping of the variation in surface atom binding energy at the nanoscale, unlocking new ways to advance the understanding of structure-property relationships in a wide range of material systems.

2 Results

2.1 Binding energy of surface atoms

APT is underpinned by field evaporation. A sufficiently high electric field is obtained by superimposing a high DC-voltage and high nanosecond voltage pulse with an amplitude of $10-25\%$ of the DC voltage. Please note that, herein, the term APT only refers to the voltage pulsed straight flight path instruments without ion optical devices (e.g. a reflectron) [30–33]. Any energy compensation [34–36] interfering with the ions trajectories removes the information that encodes the energy deficits induced by nanosecond voltage pulses.

State-of-the-art of field evaporation models interpret the passage of an atom bounded to the surface to an ion projected in a divergent field as a thermodynamic process. At cryogenic temperature $T = 20-100K$, the atom overcomes a low energy barrier of few tenths of an electron-volt by the application of a strong electric field F near the critical field F_{EV} [37].

Ab-initio calculations [38–42] indicated that the full assessment of this energy barrier $Q(F)$is possible, but remains challenging. Indeed, the relaxation of surface atom positions under the strong stress of the Maxwell forces induced by the surface field is necessary at each step of the computation [37]. Non-linearities of $Q(F)$ linked to the path of the ion at the surface during the escaping process has been reported experimentally [43] and predicted [38–42],

but only under a low applied field ($F < 0.85F_{EV}$) which is not typically used in APT. Since the specimen is maintained at a cryogenic temperature and atoms are removed from the surface for an applied field very close to the critical field [37], the evolution of the energy barrier $Q(F)$ can be approximated by a linear function (equation 1).

$$\begin{cases} Q(F) = C(1 - \frac{F}{F_{EV}}) \\ \Phi = exp(\frac{-Q(F)}{k_B T}) \end{cases} \tag{1}$$

Experimentally, the field evaporation process is described by the Arrhenius law [1] (equation 1). By precisely measuring the evaporation flux as a function of the specimen's base temperature and applied field, the binding energy of surface atoms can be evaluated. This latter parameter influences the field evaporation sequences in APT experiments.

Data were already reported for W [44] and Rh [45] for temperatures up to $100K$ and both show the predicted linear decrease of $Q(F)$ with F over $0.85F_{EV}$. We also performed a series of APT experiments on a pure Al specimen at increasing temperatures from $25K$ to $100K$ to verify the linearity of Q(F) (Supplementary Information 1). The asymptotic zero field energy barrier C can be extracted from $Q(F)$ experimental graph (Supplementary Information 1). However, this method requires dedicated and meticulous experiments, is only applicable for pure metals and the user must consider variations from one specimen to another. We therefore looked for alternatives to evaluate this factor C.

In APT, it is commonly assumed that the ions leave at the maximum of this pulse and are accelerated to their final velocity (within a nanosecond) and then collected by the detector (Supplementary Information 2). The energy conservation law is therefore used to define the species by identification of the mass peak [2]. In reality, the atoms are field evaporated following the Arrhenius law (equation 1) and the majority leave around the maximum of the pulse, that exhibit a small energy deficit δ [46]. Thus, the evolution in the mass-to-charge ratio compared to the expected value from the known element's isotopic mass M_0 can be directly provided by the estimation of δ (Figure 1), since this error is larger than any other sources of errors such as timing uncertainty [46]. This leads to mass peaks with a well-known tail decaying over several percent relative to M_0. The shape of each elemental mass peak is hence intrinsically dependent of the energetic evaporation parameter noted $a = -C/k_B T$ [47] and thus represents an image of the energy barrier as function of the field $Q(F)$ (Supplementary Information 2).

Figure 1 is a qualitative representation of the field evaporation of an atom departing from four different surface neighborhoods. Because of the different local atomic environment, the binding energy C_x of the considered atom is different, leading, cumulatively, to mass peaks with slower or faster decay, which can be approximated by linear slope a on a log scale [47]. Since the analysis temperature is assumed constant during the experiment, the value of C can be directly extracted, for instance here $C_1 > C_2 > C_3 > C_4$.

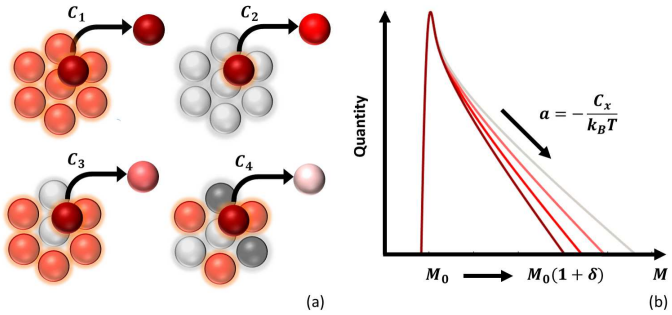

Fig. 1 (a) Qualitative representation of field evaporation of an atom depending the surface structure given different binding energy C_x. C_1: the configuration corresponds to a pure material. C_2: the configuration corresponds to a solute atom in a matrix. C_3: the configuration corresponds to a binary structure. C_4: The configuration corresponds to a ternary structure. The list of configuration is none exhaustive. (b) Qualitative form of the corresponding mass peak to the field evaporation sequence. The mass peak tail involves as function of the energy deficit δ induced by the voltage pulse. The mass peak presents a linear tail in log scale with a slope factor of $a = -C_x/k_BT$. In this example, a depends on the binding energy C_x since the temperature T is considered constant. We consider $C_1 > C_2 > C_3 > C_4$.

If the crystal structure is uniform for a pure material (*e.g.* Figure 1.a, C1), the variation of the temperature T leads to a modification of the mass peak slope that is measurable.

We have applied our proposed method on different pure metals by using a model to fit the slope parameter $a = C/k_BT$ to the experimental mass peak shapes (Supplementary Information 2). We have extracted the C factor for pure Al analyzed at $20K$ to $100K$.Because there was no previous report of Q(F) for Al, we also used the experimental method discussed above for comparison (Supplementary Information 1). We obtained comparable results and estimated a value of $0.5 \pm 0.1eV$. Al mainly field evaporates as Al^+ and Al^{2+}, we also measure the slope factor of Al^{2+} mass peak. In this case, the measurements show a very limited dependence on the charge state, as predicted by the post-ionization theory [48]. We observe a slight difference, less than 10%, which can be explained by dynamic effects caused by the voltage pulse early during the ion's flight [49] (Supplementary Information 2).

We then measured the binding energy for pure Ni and find $0.82eV \pm 0.1eV$. This value can be compared with a recent study by Hatzoglou et al [12]. who obtained an energy barrier for Ni varying from $C = 0.76eV$ in NiCu to $C = 1.17eV$ in FeCrNi, which is consistent with our value.

For W, we found $C = 1.8eV \pm 0.1eV$, i.e. slightly lower than the experimental report of Kellogg *et al.* [44] at $2.2 - 2.7eV$. The measurement done on the W^{4+} ($C = 1.8eV$) confirms also the post-ionization theory [48], since are no dynamic effects for this mass category of ions. [49].

Note that our proposed method of evaluation of this binding energy C is dependent on the linearity of the mass peak tail, the level of background towards the base of the mass peak and the error on the measurement of the

specimen's temperature (±10%). We also assumed that the energy barrier on the top of the pulse (*i.e* $F = F_{EV}$) values $0eV$, whereas it remains 0.1 to $0.2eV$, which can induced a shift in the value. We estimate the uncertainty on the measurement of C to be approximately (±10%). However, the approach we introduced herein has the advantage of being applicable broadly to existing APT . It provides a quick and accurate assessment of the field evaporation conditions across a reconstructed dataset.

2.2 Local measurement of the binding energy

In alloys, the field evaporation process depends on the atoms that constitute the material and on local structures, such as precipitates. Thus, the evaporation field of one phase may be higher (or lower) than the other, and is closely related to the binding energy of the atoms [8, 11, 50]. Here we showcase this in the analysis of an AlAg alloy containing Ag-rich precipitates after extracting the mass spectra of the Ag-rich precipitates (figure 2.a) and Al-rich matrix (figure 2.b).

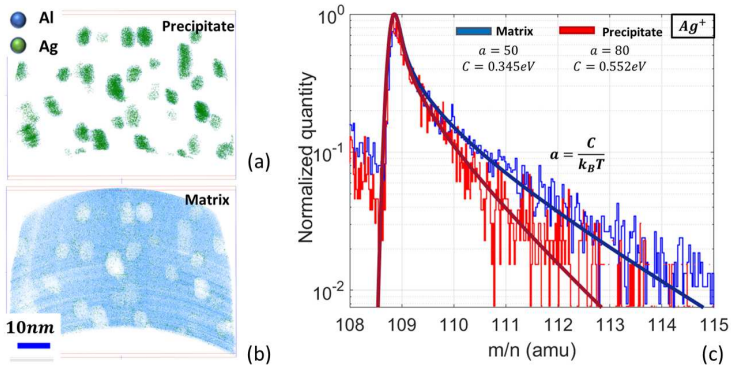

Fig. 2 Experimental results of AlAg analyzed at $T = 80K$ with a pulse fraction of 20%. (a) Visualization of the AlAg precipitate. (b) Al matrix with a residual amount of Ag (< 2%). (c) (blue) The slope factor $a = 50$ gives a binding barrier $C = 0.345eV$ for Ag atoms in the matrix. (red) The slope factor $a = 80$ gives a binding barrier $C = 0.552eV$ for Ag atoms in the precipitates.

Figure 2.c shows the mass peaks of Ag^+ from these two regions. The mass peaks tail slope are clearly different. The binding energy C is 60% higher in the precipitate than in the matrix. This difference is less visible for Al^+ mass peaks, around 4% higher in the Al-rich matrix (Supplementary Information 3).

Similar measurements were done in the analysis of an AlLi alloy containing Li-rich precipitates. Again, the binding energy of Li or Al atoms differ as function of the local structure (Supplementary Information 3). In these latter measurements, we should consider dynamics effects [49] that influence the measurement by enlarging the Li^+ and Al^{2+} mass peak tails, so that we underestimate the real binding energy.

2.3 Introducing FEELS: analysis of a structural defect

Since the precision our measurements of the binding energy C is related to a quantity of atoms contained in a mass peak tail, voxelization should allow for measuring the variation of C across an APT volume. This simple approach is what we termed as field evaporation energy loss spectroscopy (FEELS). A difference of only tens of atoms between two mass peak tails can be sufficient to reveal a change in C by several percent (see detailed discussion in Supplementary Information 4). Because these measurements are done locally, the data processing algorithms typically used on commercial instruments (*i.e.* bowl and voltage corrections [9]) do not influence the measurement. However, some errors can appears on the limits of the analysed volume, *i.e.* edges of the detector, due to poorer counting statistics.

We first revisited the APT analysis of a $\Sigma 3[110](111)$ grain boundary, *i.e.* a region separating two grains of similar crystal structure, in pure Al specimen [51]. In the reconstructed volume (Figure 3.a), the grain boundary is made visible by a lower point-density caused by trajectory aberrations [52]. Previous report on this specific dataset [51] showed no change in composition at the grain boundary itself. Figure 3.b corresponds to the mass spectra plotted in each two regions-of-interest identified in blue and in red in the inset. The slope is identical over most of the mass peak, but strongly differ above $27.75amu$, showcasing an increased energy loss for atoms on the grain boundary. FEELS is sensitive enough to reveal the difference in the field evaporation process between the grain boundary and the metallic matrix, and can hence image structural defects. This is supported by ab initio calculations of the field evaporation at the grain boundary, as detailed in Supplementary Information 5, that show different Q(F) evolution depending on the field evaporation sequence, leading to a similar evolution of the mass peak tail.

FEELS imaging maps the chemical and/or structural changes across the reconstructed volume: the relative quantity of ion contained in the tail, *i.e.* with a high energy loss denoted Al_{HEL}, compared to the rising edge of the mass peak Al_{LEL}, *i.e.* with a low energy loss (Figure 3.c) can be visualized in three-dimensions on a nanometer resolution (Figure 3.d).

2.4 Applying FEELS: highlighting structural changes

We now used FEELS on a FeBSi metallic glass, crystallized by annealing at 900°. After an identification of the constituents in the mass spectrum, we reconstructed the volume and extracted mass spectra from a B-rich FeB phase (blue) and a Si-rich FeSi phase (green) from two identical sub-volume inside each phase (Figure 4.a). The Fe mass peak tails from the two phases in Figure 4.a appear widely different, evidencing differences in the C value and hence field evaporation behavior of between the two phases. The FeB phase is crystalline, but field evaporation proceeds experimentally by burst, indicating a complex process of erosion. In FeSi phase, evaporation appears more controlled, as it was observed in FIM [53].

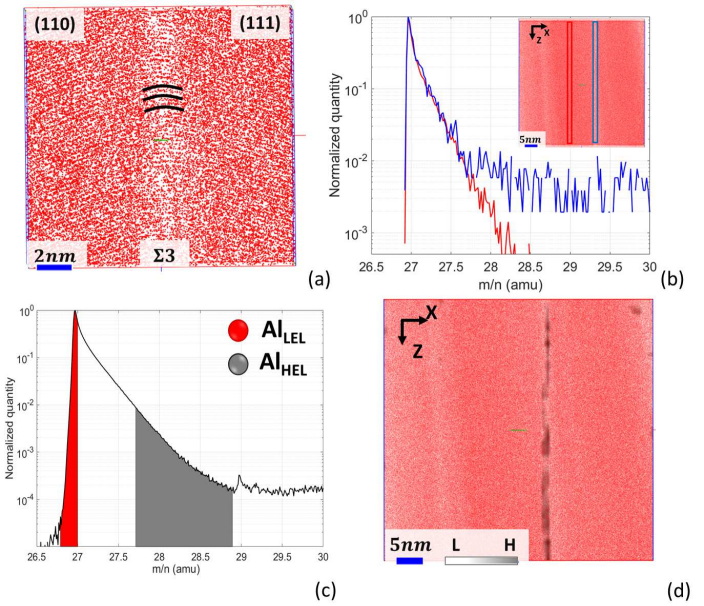

Fig. 3 Experimental result of a Σ3 Al[110](111) analysed at $60K$. (a) Reconstructed volume. The grain boundary present a low density of atoms and a curvy atomic arrangement may be due to rolling-up effects. (b) Al^{+} mass peaks of associated to the two selected volumes inside the volume: (blue) in the grain boundary, (red) in the crystal.(c) Al^{+} mass peak from the volume. (red) Al_{LEL} atoms with low energy loss (LEL) (grey) Al_{HEL} atoms from the tail, with high energy loss (HEL). (d) FEELS representation of the grain boundary after applying a plane projection of the Al_{HEL}/Al_{LEL} composition map to increase the visibility.

The rolling-up motion of atoms on the surface of FeB phase prior to field evaporation may also be more pronounced [11, 22]. This is reflected by the presence of a larger tail of Fe^{2+}, *i.e.* higher energy loss compared to the FeSi. Considering the mass spectrum of the entire dataset (Figure 4.b), Fe from the rising edge of the mass peaks, Fe_{LEL} in red, are mostly contained in the FeSi phase; whereas atoms that belong to the Fe tail, Fe_{HEL} in grey, are segregated into the FeB phase (Figure 4.b).

Surprisingly, FEELS also highlights the presence of a grain boundary inside the FeSi phase (figure 4.c), *i.e.* enabling to perform structural analysis that can be elusive to conventional APT. A 3D-reconstructed volume, Supplementary Information 6, reveals the entire FeBSi structure imaged by FEELS. Another example of application on a FeBSi sample annealed at 500° is presented in Supplementary Information 7. In this experiment, we were expected two crystalline phases FeSi and FeB, however FEELS reveals us a third structure. The composition measurement shows no distinction with a FeB phase, so we believe that the crystalline structure is locally different. Further studies are engaged to verify this hypothesis.

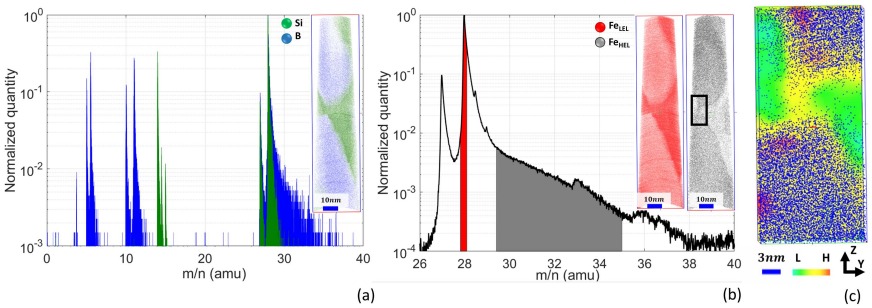

Fig. 4 Experimental result of a FeBSi annealed at 900° analysed at $50K$. (a) Reconstructed volume: (green) Si in FeSi phase, (blue) B in FeB phase. The corresponding phase mass spectrum are plot : (green) FeSi, (blue) FeB. (b) FEELS utilisation on Fe^{2+} mass peak of the entire dataset: (red) Fe_{LEL}, (grey) Fe_{HEL}. (black square) Visualisation of the FeSi grain boundary by the FEELS method. The FeB phase and the grain boundary show a high energy loss of Fe. (c) FEELS representation of the FeSi grain boundary (visible yellow on colormap). Blue dots represent B atoms in the Fe2B phase.

3 Discussion

To summarize, the mass peaks in APT are not only useful to identify elements and count atoms, but their shape encodes information regarding the binding of an atom with its neighborhood and the energetic aspects of the field evaporation process. We have introduced FEELS to map changes in the energy barrier for field evaporation on the nanometer scale. We have showcased the possibility to discriminate precipitates from a matrix, structural defects their surroundings, and enabling to reveal microstructural details that were elusive to conventional APT analysis. In the configuration of the state-of-the-art instruments (LEAP 5000XS), measurements are reliable for a wide range of elements with a mass-to-charge ratio above $15amu$, below which the dynamic effects associated to the voltage pulse amplify the error. FEELS offers wide possibilities to revisit and complement conventional APT analyses, in particular in search for possible microstructural features including structural defects that had remained hidden within existing data and could hence be targeted for structural and compositional analyses.

4 Methods

The pure tungsten specimen was prepared from a wire oriented, along the $< 011 >$ direction, and prepared by electrochemical-polishing with a solution of 5% NaoH in water with a voltage in the range of $1 - 5V$. Pure Al specimen was prepared using electropolishing method with $1 - 10\%$ perchloric acid in methanol with a voltage in the range of $5 - 8V$. Pure Ni specimen was prepared using electropolishing method with 10% perchloric acid 70%, 20% glycerol in ethanol. The final step is done with 2% perchloric acid in 2-butoxyethanol. The voltage range is $22V$. Further details on electropolishing method can be found in literature. [14, 54, 55]

The $\Sigma 3[110](111)$ grain boundary volume comes from a pure Al (> 99.99%) used to form bi-crystals via the Bridgman technique. The crystals were sectioned using a diamond wire saw into rectangular blocks that were 3 mm long, 1 mm wide and 500 μm thick. The grain boundary was placed end on when looking at the 3x1mm face, and 45° away from the longest axis of the block. One 3x1 mm face was mechanically polished for a few tens of microns using 1200 and then 4000 grit SiC paper. The block was then dipped into an aqueous solution of HNO_3, HCl and HF to optically reveal the GB. Further information can be found in [51].

The AlAg alloy was prepared with $Al - 3at.\%Ag$ aged at $300°C$ for 3 min, which produced 8-to 15-nm-diameter GP zones containing $34at.\%Ag$. The specimens were prepared using standard electropolishing solutions. Further information can be found in [8].

The AlLi alloy was annealed for 8h at 500°. The needle-shaped specimens were then fabricated by electropolishing in a solution of 25% perchloric acid in glacial acetic acid with a $10 - 12V_{DC}$, followed by a second stage of fine polishing under a binocular microscope with 2% perchloric in 2-butoxyethanol with a $20 - 25V_{DC}$. Further information can be found in [56].

The FeBSi metallic glass alloy initial composition is 77.5% of Fe, 15% of B and 7.5% of Si. The specimen originally presents an amorphous structure that was crystallized at $500°C$ or $900°C$ during an hour. Needle shape specimen were prepared by "lift-out" and annular milling" using using a xenon plasma-focused ion beam (FIB) instrument [14, 54, 55].

Atom Probe experiments were done using straight flight path LEAP series [57] in classical conditions. The voltage pulse fraction was 15% or 20% and the applied temperature was under $100K$.

Supplementary information.

- Binding energy of Al atoms in pure Al specimen
- Evaluation of the mass peak shape
- Local measurement of the binding energy
- Statistical error on FEELS technique
- Complementary information on Aluminium grain boundary
- 3D-FEELS on FeBSi annealed at 900°C
- FEELS on FeBSi annealed at 500°C

Acknowledgments. We thank Uwe Tezins, Christian Broß, and Andreas Sturm for their support to the FIB and APT facilities at MPIE. L.T.S. and B.G. acknowledge financial support from the ERC-CoG-SHINE-771602. F.F.M. acknowledges financial support from the International Max Planck Research School for Interface Controlled Materials for Energy Conversion (IMPRS-SurMat).

Appendix A Binding energy of Al atoms in pure Al specimen

Field evaporation is described as a thermally activated process [58]. Atoms are originally confined in an energetic well of a certain height ($Q(F) = 1 - 3eV$). Under the effect of this intense electric field ($F = 20 - 60V/nm$), the energy barrier Q(F) decreases to a fraction of electron-volt. The thermal agitation of the surface atoms allows them to overcome an activation energy barrier and escape the surface in the form of a singly-charged ion that can undergo further ionisation in the early stages of its flight [48]. This process is experimentally translated by a classical Arrhenius law [37], in which the field evaporation flux is dependent on the temperature T applied to the sample and on the bounding energy $Q(F)$, that the atom need to cross in order to be field evaporated. In the APT community, standard analyses are realised for an electric field $F > 0.8F_{EV}$ and at low temperature ($20 - 80K$). Thus, the most common approach to evaluate $Q(F)$ is to suppose a linear decrease (equation 1) and estimate the zero-field energy barrier C.

The method is as follow. For each measurement, we counted 30 000 atoms. The mass peaks are presented on the figure B7.a. For the four temperatures from $25K$ to $100K$, the electric field required to evaporate the atoms is evaluated at different detection rates DR from 0.05% to 1%. A linear correction in tension is applied to take into account the enlargement of the apex of the tip. This allows to obtain the graph on figure A1.a. We do not consider the value at $DR = 0.05\%$, because at low flux the atoms are more likely to move on the surface before evaporation by field effect. This increases the uncertainty on the evaporation time. To simplify the extraction of the binding energy height, the data are fitted with a linear equation (equation A1), the slope of which extracts the coefficient C.

$$f(\frac{F}{F_{EV}}) = ln(DR_{\%}) = ln(\phi) = \frac{Q(F)}{k_B T} + C_1 \tag{A1}$$

At the same evaporation field $F = 0.85F_{EV}$ (figure A1.a, black arrow), we have a difference in detection rate by a factor of 10 for two temperatures of $100K$ and $80K$. By solving the equation A1, we obtain the first value: $C = 0.8eV$. Then, assuming that the height of the energy barrier varies linearly with temperature, the other coefficients are defined for the highest and lowest detection rates.

Finally, it is possible to plot the evolution of Q(F), represented in green on the figure A1.b. Experimental measurements of W [44] and Rh [45] are added for visual comparison of Q(F) evolution.

Comparing these Al values with those of the table A1, we observe similar results with our method consisting in evaluating the slope of the mass peaks

This result demonstrates (figure A1, green), that the energy barrier measured experimentally is well described by a linear evolution, which can be

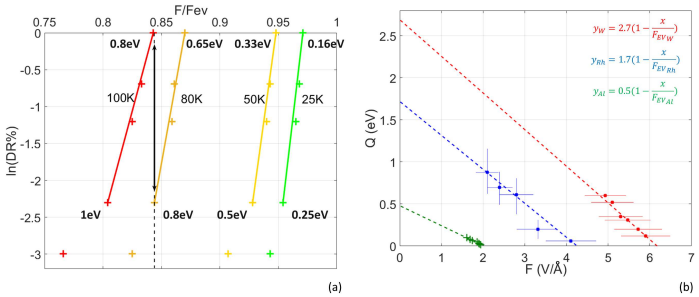

Fig. A1 (a) Experimental data of detection rate versus field for Al^+ at (red) 100K, (orange) 80K, (yellow) 50K and (green) 25K performed on a LEAP5000XS. The evaluation of the binding energy at different measurement conditions is added. (b) Experimental data of the evolution of the energy barrier as a function of the field evaporation for experimental result for (green) Al, (blue) Rh [45] and (red) W [44]. Each point corresponds to a temperature at which the barrier $Q(F)$ is measured for a corresponding field evaporation F. In dotted line, it is presented the linear equation following the equation 1

Table A1 Experimental measurement of the slope factor C/k_BT and extraction of C for Al specimens relative to figure 1.b

Ions	M (amu)	Temperature(K)	Coefficient $\frac{C}{k_BT}$	C(eV)
Al^{2+}	13.5	25	95	0.204
		50	80	0.344
		80	65	0.414
		100	40	0.344
Al^+	27	25	120	0.25
		50	90	0.387
		80	70	0.48
		100	60	0.517

modeled by the equation 1. The zero-field energy barriers C for the different specimens are: $C_W = 2.7eV$ [44], $C_{Rh} = 1.7eV$ [45], $C_{Al} = 0.5eV$.

Appendix B Evaluation of the mass peak shape

The field evaporation is triggered by the voltage pulse. In theory, it is considered, that the ions leave towards the detector, when the pulse is at its maximum at t_0. Then their impact on the detector gives the time-of-flight t_f. The initial velocity is null and the acceleration period between the tip and the counter-electrode ($t < 1ns$) is neglected compared to the time-of-flight ($t_f > 100ns$). Thus, ions acquire almost instantaneously all the kinetic energy E_k induced by the potential energy E_p. Then the experimental mass-to-charge

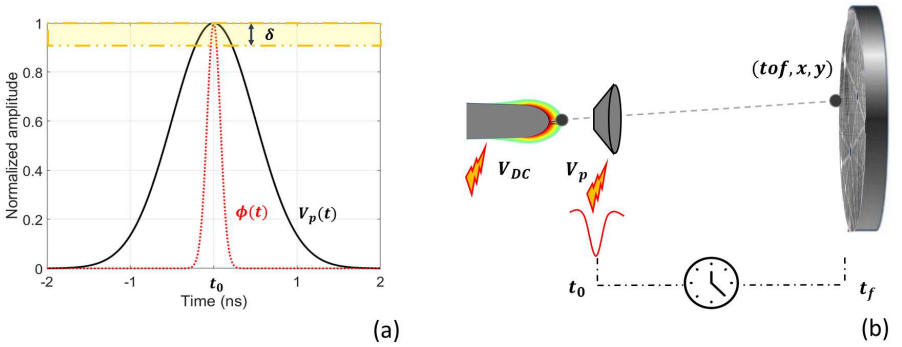

Fig. B2 (a) Normalised voltage pulse $V_p(t)$ (black) and (red) field evaporation flux $\phi(t)$ following equation 1. Majority of atoms are field evaporated at $0.9V_P$ with a small energy deficit $ne\delta$ compared to the maximum of energy E_p. (b) Schematic of APT time-of-flight mass spectrometry principle. Ions are field evaporated at t_0, the maximum of the voltage pulse. Time-of-flight corresponds to the time t_f of the impact on the detector corrected by t_0. [59].

state ratio ($M = m/n$) is determined using the conservation of energy law $E_c = E_p$ (equation B2) [59].

$$M = \frac{m}{n} = 2eV\frac{tof^2}{L^2} = 2e(V_{DC} + V_p)\frac{(t_f - t_0)^2}{L^2} \tag{B2}$$

The real time-of-flight (tof) is defined by the time (t_f) corresponding to the recording of the impact on the detector corrected by the time departure (t_0) synchronised with the maximum of the pulse. The voltage pulse is define as $Vp = f_p V_{DC}$ where f_p represents the pulse fraction. L is the flight distance between the tip and the detector. e is the electronic charge and n corresponds to the charge state[2].

Note that the charge $n = 1^+, 2^+, 3^+$ *etc.* comes from the number of post-ionization that the ion has undergone. It can be predicted thanks to the Kingham curves [48].

B.1 Qualitative solution

In reality, the field evaporation is modelled by the Arrhenius law (equation 1), that gives a small uncertainty on the time departure dt of the atoms. Indeed most of the atoms are field evaporated near the maximum of the pulse with a small energy deficit δ, so that the real voltage V corresponds to equation B3.

$$V = V(1 - \delta) \tag{B3}$$

The atom probe uses the time-of-flight mass spectrometry principle to determine the mass-to-charge state ratio of the detected ions [59]. If we consider the dispersion error on the time departure ($dt < 200ps$, for a voltage pulse width of $1ns$) negligible compared to the ion time-of-flight (t_f), then the equation B2 becomes (equation B4) :

$$\frac{m}{n} \approx 2eV(1-\delta)\frac{tof^2}{L^2} \tag{B4}$$

If we note the theoretical value $M_0 = m_0/n_0$ associated to the detected element, the evolution at the first order of the experimental mass M as function of the energy deficit δ corresponds to equation B5.

$$M \approx M_0(1+\delta) \tag{B5}$$

This expression allows us to plot the following mass peak (figure B3, left). Its height corresponds to a quantity of atoms that is closely related to the field evaporation flux ϕ (equation 1). The evolution of the mass peak tail depends on the energy deficit δ created by the voltage pulse.

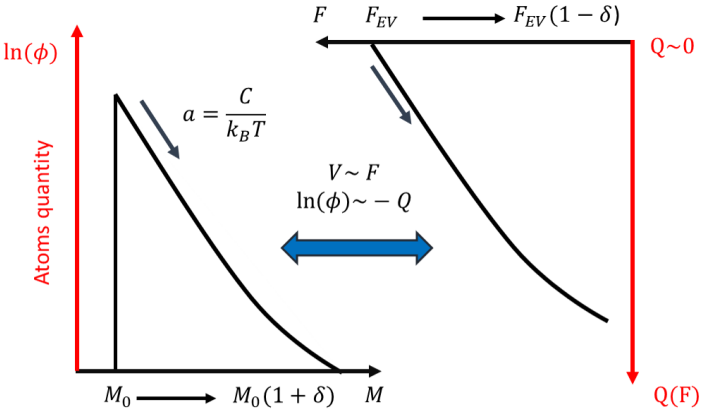

Fig. B3 (a) Qualitative mass spectrum shape evolution. The ion quantity that constituted the peak is relied to the logarithm of the field evaporation flux (equation 1). The mass peak tail evolution is dependent of the energy deficit δ. However, the field F evolution at the apex is proportional to the voltage V applied on the sample and the field evaporation flux ϕ is relative to the field energy barrier $Q(F)$. This representation shows a close relation between the mass peak tail evolution and the field energy barrier evolution.

As we noticed, the evolution of the field F around the tip apex is proportional to the applied voltage V (equation 1). Thus, the energy deficit δ from equation B3 also corresponds to (equation B6):

$$\delta \approx 1 - \frac{F}{F_{EV}} \tag{B6}$$

From this equation B6, it possible to write equations 1 and B4 as function of δ to trace the equivalent distribution of the field evaporation flux ϕ and of the energy barrier Q (figure B3, right). This qualitative solution shows that the mass peak tail evolution is closely related to the energy barrier $Q(F)$, that is intrinsic to the material.

B.2 Analytical solution

The mass peak shape is related to the energy deficit. An analytical solution was calculated by Zhao *et al.* [47] from the field evaporation flux (equation 1). Thus, authors determined the theoretical energy distribution D_δ^F of the field evaporated atoms (equation B7).

$$ln(\phi) \approx D_\delta^F = \frac{exp(-a\delta)}{\sqrt{\pi a \delta}} \tag{B7}$$

From this equation B7, it is possible to trace the resulting energy distribution D_δ^F as function of the energy deficit δ .

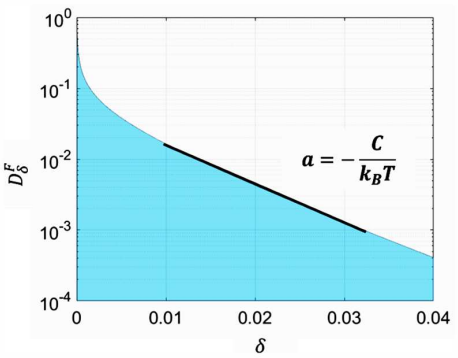

Fig. B4 Energy distribution D_δ^F calculated from equation B7 with $\delta = 1/50000$. In log scale, the tail of the peak can be approximated by a linear equation of slope factor $a = -C/k_BT$.

Figure B4 shows that the energy deficit distribution has a linear tail that has a negative slope factor $a = C/k_BT$. From this study, we can notice that the experimental mass peak tail gives an indication of the height of the energy barrier C, considering the knowledge of the temperature of the analysis T.

B.3 Influence of the dynamic effects

In reality, we should consider additional factors that modify the mass peak shape. Those are dynamic effects [49]. When the atoms are field evaporated near the maximum of the voltage pulse, the field around the tip apex is still varying. Thus, after the acceleration period ($< 1ns$), the voltage pulse is not ended and it exists a residual negative field after the counter electrode, that implies strong velocity variations. As shown on the following graph (figure B5), two consequences are created by those dynamics effects. Firstly, the maximum of the kinetic energy (E_K) is not centered on the maximum of the potential energy (E_P). There is a small temporal shift. Secondly, the ion deceleration after the counter electrode increase the energy deficit. That is why the amplitude of the kinetic energy (E_K) is lower than potential energy (E_P).

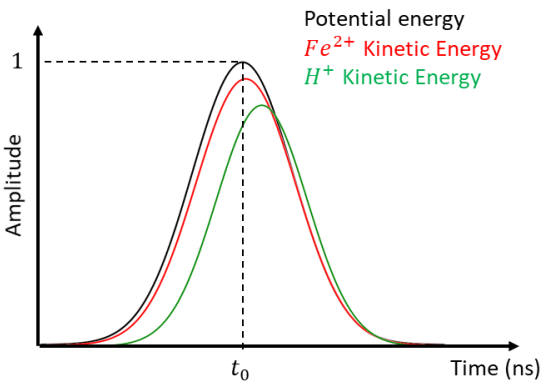

Fig. B5 (black) Energy potential, (red) Fe^{2+} kinetic energy, (green) H^+ kinetic energy. Dynamic effects create a temporal shift of the maximum of the kinetic energy compared to the potential energy and increase the energy deficit.

In order to establish an accurate evaluation of the mass peak slope factor, we simulated the trajectories on Lorentz-2E [60] for a : H^+, B^{2+}, Al^{3+}, B^+, Al^{2+}, Si^{2+}, Al^+, Fe^{2+}, W^{4+}, W^{3+}, W^{2+} for two voltage pulse fraction $f_p = 10\%$ (figure B6, blue) and $f_p = 20\%$ (figure B6, red). Then we calculate [47] the corresponding mass peak by arranging the equation 1, to find the coefficient $a = C/k_BT$ that is imposed to a value $a = 200$. This is equivalent to an experiment realised on a material whose energy barrier is of $C = 1eV$ analysed at a temperature of $T = 80K$. The Boltzmann constant is of $k_B = 8.617.10^{-5}eV.K^{-1}$. As an example, figure B6 a,b show the results for the mass peaks of H^+ and Fe^{2+}. The dynamic effects are depends of the ion mass. They are more important for lower ion the mass (ex: H^+).

The figure B6.c shows the evolution of the slope factor measurement realised using the equation B8 [46].

$$ln(D_N) = \frac{1}{2}ln(\frac{C}{k_BT}) - \frac{1}{2}ln(\delta) - (\frac{C}{k_BT})\delta \tag{B8}$$

In logarithmic scale, this equation B8 is mainly composed of a negative slope factor whose coefficient is $a = C/k_BT$.

Following the figure B6.c, we see that the dynamic effects are strongly visible for a range of light mass ions from 1 to $15amu$, and can be amplified by the voltage pulse fraction. For higher mass, the measurement of the theoretical value $a = 200$ is stable at $\pm 10\%$ due to the exponential linear regression method approximation. Thus the actual LEAP 5000XS [57] is optimised for ions with mass-to-charge state ratios greater than $15amu$. It means, that the extraction of the experimental mass peak slope factor will give an accurate estimation of the energy barrier. For other species, this evaluation quickly becomes uncertain.

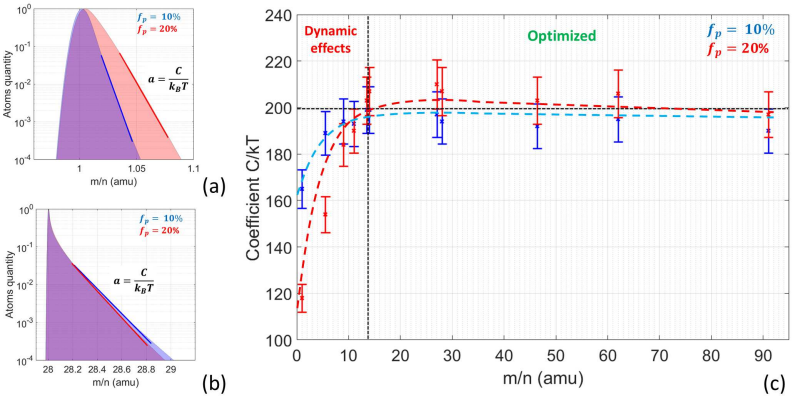

Fig. B6 (a) H^+ Mass peak. (b) Fe^{2+} Mass peak calculated after ion trajectory simulation on Lorentz-2E [60]. (c) Measurement of the mass tail slope factor for different ion using different voltage pulse fractions $f_p = 10\%$ (blue) or $f_p = 20\%$ (red) applied on the counter electrode. The expected slope $C/k_BT = 200$ is represented by a black dotted line. The percentage of error on each point is 10%. The dotted lines represent a visual guide

B.4 Experimental application on pure material

As an application example, we apply a model (Figure B7, blue area) issued from equation B8 to evaluate the different experimental mass peak tail slope factor presented in the paper.

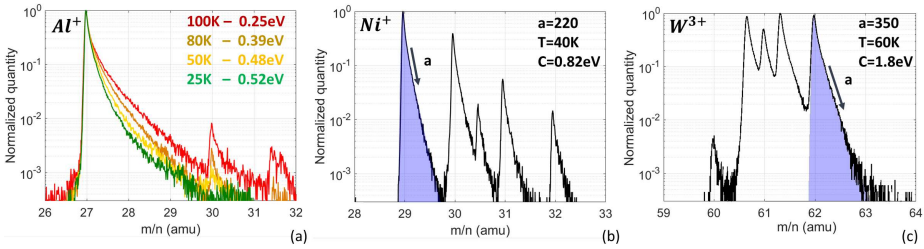

Fig. B7 (a) Experimental mass peaks of Al specimen analyzed at $T = 25 - 100K$. The slope factors $a = 60 - 120$ give binding energies $C = 0.25 - 0.52eV$. (b) Experimental mass peak of Ni specimen analyzed at $T = 40K$. The slope factor $a = 220$ gives a binding energy $C = 0.82eV$. (c) Experimental mass peak of W specimen analyzed at $T = 60K$. The slope factor $a = 350$ gives a binding energy $C = 1.8eV$

Appendix C Local measurement of the binding energy

The following table C2 shows local measurements of the binding energy C in AlAg and AlLi alloys.

Table C2 Experimental measurement of the slope factor C/k_BT for Ni, Al, Li

Ions	M (amu)	Material	Structure	Temperature(K)	Coefficient $\frac{C}{k_BT}$	C(eV)
Li^+	7	AlLi	Matrix	40	110	0.379
			Precipitate		110	0.379
Al^{2+}	13.5		Matrix		200	0.689
			Precipitate		220	0.758
Al^+	27		Matrix		220	0.758
			Precipitate		210	0.724
Al^{2+}	13.5	AlAg	Matrix	80	130	0.896
Al^+	27		Matrix		125	0.862
			Precipitate		120	0.827
Ag^+	107		Matrix		50	0.345
			Precipitate		80	0.552
	109		Matrix		50	0.345
			Precipitate		80	0.552

Appendix D Statistical error on FEELS technique

FEELS technique is essentially based on the atoms counting accuracy, so that our technique is limited to a certain statistic error degree. This section express the limit of validity of our measurement.

From previous studies [47], the normalized quantity of atom N_{at}/N_t as function of the energy deficit (δ) directly informs on the atom quantity that are contained in the mass peak tail (equation D9).

$$\frac{N_{at}}{N_t} = 1 - erf[(a\delta)^{1/2})] \tag{D9}$$

In the following example, we consider 1 millions of Al atoms that are homogeneously distributed in a cubic volume of $25nm$. In the center of this volume, we consider a sphere of a radius of $2nm$. The objective of this theoretical simulation is to define the minimum binding energy difference between atoms from the matrix and the spherical cluster, to be able to discriminate this two structures by using FEELS methods. Thus we fix the a factor $a = 100$ to atoms in the matrix and change the one in the cluster, so that it correspond to different binding energy, since T is the same in all the volume. Then by using equation D9, it is possible to extract corresponding mass peak for each volume (figure D8.a) and then calculate the total mass peak (figure D8.b). On the total Al mass peak, we define as Al_{HEL} atoms that have high energy loss compared to Al_{LEL} atoms that have low energy loss. The limit of the two area in the mass peak is set at an energy deficit $\delta = 1\%$ of $M = 27amu$.

As we can see, it is impossible to visualise the two structures in the classical reconstruction method (figure D8.c). On this example, we find that a difference of binding energy of 30%, i.e. $a = 70$ in the sphere, is sufficiently high, to either make the FEELS cartography or having Al_{HEL} atoms composition reliable (figure D8.e). Indeed, if we consider a $1nm$ box composition measurement, a statistical error of 2σ must be considered.

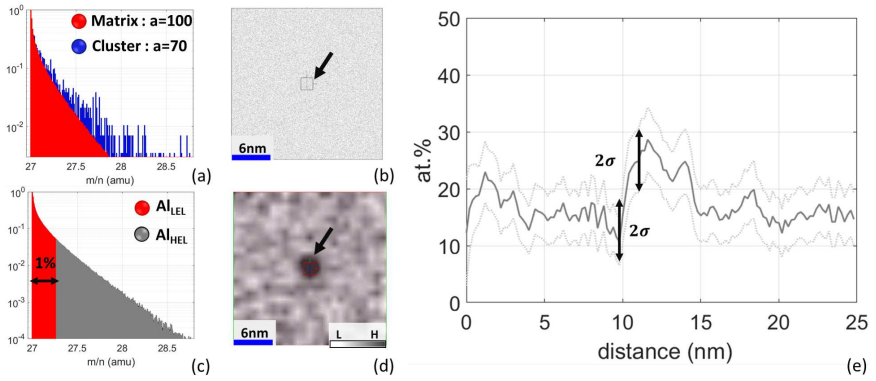

Fig. D8 Simulation of a spherical cluster (Radius=2nm) of Al, inside an Al matrix (size=25x25x25nm). (a) Corresponding Al mass peak. (b) Identification of Al_{HEL} at a deficit $\delta = 1\%$ of Al_{LEL}. (c) FEELS representation of Al mass peak after evaluation of Al_{HEL} over Al_{LEL} composition. (d) Composition measurement of Al_{HEL} with a box of $1nm$ and moving step of $0.2nm$ in the center of the volume (black arrow)

We did other simulation, where the radius of the spherical volume is changed to $1nm$. The difference of binding energy between the two structure must be over 50% to be visible by FEELS.

Appendix E Complementary information on Aluminium grain boundary

To validate the difference in the evolution of the energy barrier between the grain boundary and the rest of the volume, a density functional theory (DFT) study was carried out. The methodology used is similar to that developed by Ashton *et al.* [41]. The grain boundary is modeled (figure E9.a) periodically by a stack of atoms (A,B,C) defining the sequence of each of the two grains composed of six rows. The first crystal has the sequence ABC (green), the second crystal has the sequence BAC (orange). The rows are tilted to give the two crystallographic orientations (110) and (111) represented by the green and orange lines. The rupture of the sequences highlights the location of the two grain boundaries CB and CA (red letters).

In order to realise $Q(F)$ model, four different surfaces A30, B30, C30, D30 are modeled with one or more protruding atoms (A, B or C). Then different evaporation sequences are calculated, for example the sequence B30a shows the evaporation phenomenon of the B atoms from the B30 plane giving the following A30 plane. The directions of the surface motions (rolling-up) of the atoms during the sequences are highlighted (blue letters) on the figure E9.a. The result of these DFT simulations is shown on figure E9.b by plotting the evolution of the energy barrier Q as function of the applied electric field F.

It is possible to observe equivalent behaviors in the sequences (*e.g.* $A30b = D30c$), as these evaporation sequences are identical. Nevertheless, it is interesting to note that the evolution of the energy barrier of the atoms,

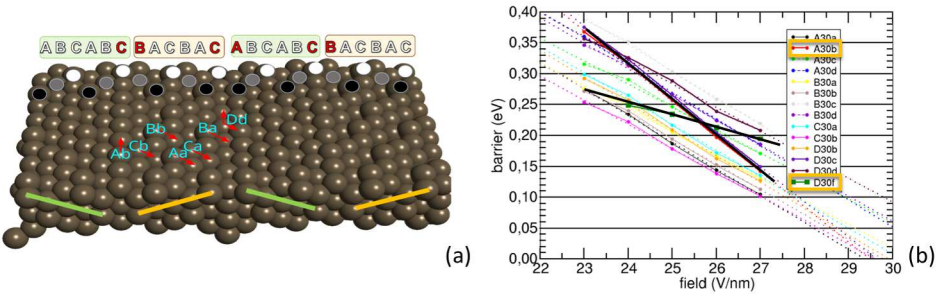

Fig. E9 (a) Model of an Al grain boundary [110](111). The sequence of atoms is defined by the letters A (black), B (gray) and C (white). The two grains are represented by a sequence of 6 rows represented in orange and green. The crystallographic orientation is highlighted by the corresponding lines. (b) Evolution of the energy barrier as a function of the field applied on the surface for different evaporation sequences. The slopes of the different evaporated atoms are quasi-linear and differ according to the sequence and the position of the atoms on the surface

really depends on the position on the grain boundary as well as the evaporation sequence. The slopes $Q(F)$ differ according to the associated field effect evaporation phenomena. For example, the D30f variation has a slope twice as small as the A30b or A30c variation, as well as a field evaporation effect twice as high.

Figure E10 highlights the link between the evolution of the mass peak train and the evolution of Q(F) on the grain boundary Σ3. As we expressed in the previous paragraph the amount of ions in a mass peak is proportional to the evaporation flux and the evolution of the tail depends on the energy deficit of the ions. Moreover, the evolution of the electric field is proportional to the voltage V applied on the sample and the evaporation flux is related to the energy barrier Q(F). This allowed us to draw the figure E10. In the present case, we have inverted the graph of figure E9 and taken the experimental results of figure 4. We find a very good consistency between the evolution of the mass peak tail and $Q(F)$.

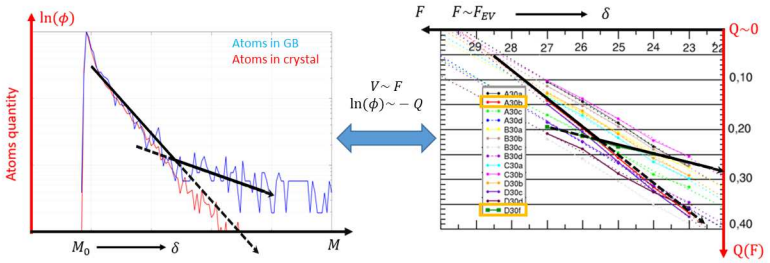

Fig. E10 (left) Experimental mass peak of Al^+ on the grain boundary (blue) and in the crystal (red). (right) This qualitative representation shows the link between the evolution of the mass peak of Al^+ and the energy barriers of Al atoms on the grain boundary.

Note that most of the Σ3 grain boundary is imaged with atoms contained between 27.5 and 29 far from the AlH2 peak. Moreover, the peak at 29amu is one order of magnitude lower than atoms contained in the tail (figure 5.a). It represents no significant atoms in the grain boundary.

Appendix F 3D-FEELS on FeBSi annealed at 900°C

Video of the 3D FEELS reconstructed volume of the FeBSi annealed at 900°C.

Appendix G FEELS on FeBSi annealed at 500°C

As a second example, we analyzed a FeBSi alloy annealed at $500°CC$. The study was performed on a LEAP 5000XS [57] at a temperature of $50K$ and a pulse fraction of 20%. After the identification of the different elements (Fe, B, Si) in the mass spectrum, we can represent the phases in the reconstructed volume. Shows the presence of silicon (green) in the FeSi phase and the presence of boron in the Fe2B phase (blue). In each phase a volume is selected to plot the associated mass spectrum of Fe^{2+} (figure G11.a). We can see that the evolution of the two tails are different. This observation demonstrates that field evaporation mechanisms are different. The annealed FeB phase is a crystalline structure, where the field evaporation is more bursty than in the FeSi phase. The rolling-up of atoms on the surface could also be more important before being field evaporated. This is reflected by the presence of a larger tail of Fe^{2+} meaning a more important energy deficit than in the FeSi crystal structure.

To realise the FEELS representation, we only consider the Fe^{2+} mass peak in the composition measurement (figure G11.b). Let us recall that this mass peak of Fe^{2+} is an accumulation of the contributions of the two previous mass peaks (figure G11.a). We identify atom from the tail Fe_{HEL} (grey) and atoms from the rising edge of the peak Fe_{LEL} (red). Then we calculate the distribution Fe_{HEL}/Fe_{LEL} in the reconstructed volume (figure G11.b).

We clearly observe the FeSi phase in red and the FeB phase in green. The first one presents the lower composition of atoms from the tail and the second one shows a more important contribution in the mass tail. These two phases are well defined and consistent with the classical reconstructed volume. By comparing this two volumes, we can also identify a third phase in blue on the spectroscopy. This one is not identifiable in the classical reconstruction. In this phase, Fe atoms are field evaporated with the highest energy deficit.

When we compute the three mass spectra (figure G11.c) for each phase and calculate the local composition, we find that the blue and green phases have a similar composition of boron and silicon. This largely explains, why the third phase is not visible on the reconstructed volume (figure G11.a). Thus the difference of the field evaporation phenomena of the Fe atoms may be come from a difference of the crystal structures. This phase may be formed

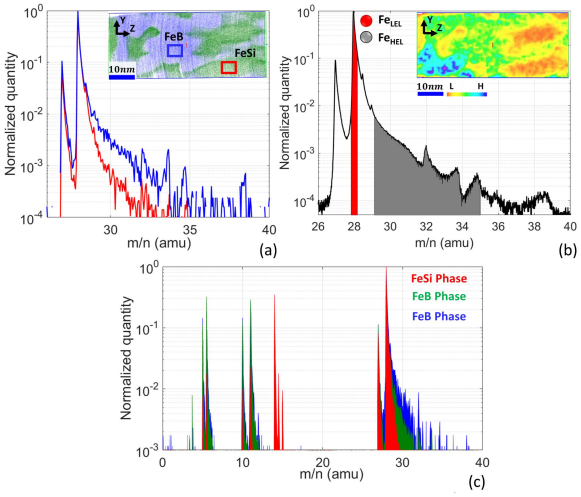

Fig. G11 (a) Classical volume reconstruction of FeBSi: Si in the FeSi phase (green), B in the FeB phase (blue). Normalised mass spectrum of Fe^{2+} associated with the FeSi phase (red) and FeB phase (blue). (b) Experimental mass spectrum of Fe^{2+}. (red) Fe at rising edge of the mass peak Fe_{LEL}, (grey) Fe in the tail of the mass peak Fe_{HEL}. FEELS representation of Fe_{HEL}/Fe_{LEL} composition. Three phases are now identifiable. (c) Mass spectrum of each three phases after FEELS identification.

as a consequence of xenon (Xe) irradiation in the border of the FeBSi volume during sample preparation. It should also be noticed that the FeBSi crystallisation was found extremely complex [61]. Further studies are engaged to better understand this phenomenon.

References

[1] D.G. Brandon, On field evaporation. The Philosophical Magazine: A Journal of Theoretical Experimental and Applied Physics **14**(130), 803–820 (1966). https://doi.org/10.1080/14786436608211973. URL https://doi.org/10.1080/14786436608211973. Publisher: Taylor & Francis _eprint: https://doi.org/10.1080/14786436608211973

[2] C. Pareige, W. Lefebvre-Ulrikson, F. Vurpillot, X. Sauvage, in *Atom Probe Tomography*, ed. by W. Lefebvre-Ulrikson, F. Vurpillot, X. Sauvage (Academic Press, 2016), pp. 123–154. https://doi.org/10.1016/B978-0-12-804647-0.00005-X. URL http://www.sciencedirect.com/science/article/pii/B978012804647000005X

[3] Atom probe tomography. Nature Reviews Methods Primers **1**(1), 52 (2021). https://doi.org/10.1038/s43586-021-00054-x. URL http://www.nature.com/articles/s43586-021-00054-x

[4] D. Haley, A.J. London, M.P. Moody, Processing APT Spectral Backgrounds for Improved Quantification. Microscopy and Microanalysis **26**(5), 964–977 (2020). https://doi.org/10.1017/S1431927620024290. URL https://www.cambridge.org/core/product/identifier/S1431927620024290/type/journal_article

[5] M.K. Miller, The effects of local magnification and trajectory aberrations on Atom Probe analysis. Le Journal de Physique Colloques **48**(C6), C6–565–C6–570 (1987). https://doi.org/10.1051/jphyscol:1987692. URL http://www.edpsciences.org/10.1051/jphyscol:1987692

[6] A. Waugh, E. Boyes, M. Southon, Investigations of field evaporation with a field-desorption microscope. Surface Science **61**(1), 109–142 (1976). https://doi.org/10.1016/0039-6028(76)90411-8. URL https://linkinghub.elsevier.com/retrieve/pii/0039602876904118

[7] F. Vurpillot, A. Bostel, D. Blavette, Trajectory overlaps and local magnification in three-dimensional atom probe. Applied Physics Letters **76**(21), 3127–3129 (2000). https://doi.org/10.1063/1.126545. URL http://aip.scitation.org/doi/10.1063/1.126545

[8] E.A. Marquis, F. Vurpillot, Chromatic Aberrations in the Field Evaporation Behavior of Small Precipitates. Microscopy and Microanalysis **14**(6), 561–570 (2008). https://doi.org/10.1017/S1431927608080793. URL https://www.cambridge.org/core/product/identifier/S1431927608080793/type/journal_article

[9] D. Larson, B. Gault, B. Geiser, F. De Geuser, F. Vurpillot, Atom probe tomography spatial reconstruction: Status and directions. Current Opinion in Solid State and Materials Science **17**(5), 236–247 (2013). https://doi.org/10.1016/j.cossms.2013.09.002. URL https://linkinghub.elsevier.com/retrieve/pii/S1359028613000739

[10] M.K. Miller, G.D.W. Smith, An atom probe study of the anomalous field evaporation of alloys containing silicon. Journal of Vacuum Science and Technology **19**(1), 57–62 (1981). https://doi.org/10.1116/1.571017. URL http://avs.scitation.org/doi/10.1116/1.571017

[11] C. Oberdorfer, T. Withrow, L.J. Yu, K. Fisher, E. Marquis, W. Windl, Influence of surface relaxation on solute atoms positioning within atom probe tomography reconstructions. Materials Characterization **146**, 324–335 (2018). https://doi.org/10.1016/j.matchar.2018.05.014. URL https://linkinghub.elsevier.com/retrieve/pii/S1044580318302225

[12] C. Hatzoglou, S. Rouland, B. Radiguet, A. Etienne, G.D. Costa, X. Sauvage, P. Pareige, F. Vurpillot, Preferential Evaporation in Atom Probe Tomography: An Analytical Approach. Microscopy

and Microanalysis **26**(4), 689–698 (2020). https://doi.org/10.1017/S1431927620001749. URL https://www.cambridge.org/core/product/identifier/S1431927620001749/type/journal_article

[13] M. Miller, M. Hetherington, Local magnification effects in the atom probe. Surface Science **246**(1-3), 442–449 (1991). https://doi.org/10.1016/0039-6028(91)90449-3. URL https://linkinghub.elsevier.com/retrieve/pii/0039602891904493

[14] B. Gault (ed.), *Atom probe microscopy*. No. 160 in Springer series in materials science (Springer, New York, 2012). OCLC: ocn775406154

[15] L. Yao, T. Withrow, O.D. Restrepo, W. Windl, E.A. Marquis, Effects of the local structure dependence of evaporation fields on field evaporation behavior. Applied Physics Letters **107**(24), 241,602 (2015). https://doi.org/10.1063/1.4937454. URL http://aip.scitation.org/doi/10.1063/1.4937454

[16] F. Vurpillot, C. Oberdorfer, Modeling Atom Probe Tomography: A review. Ultramicroscopy **159**, 202–216 (2015). https://doi.org/10.1016/j.ultramic.2014.12.013. URL https://linkinghub.elsevier.com/retrieve/pii/S0304399114002708

[17] F. De Geuser, B. Gault, Metrology of small particles and solute clusters by atom probe tomography. Acta Materialia **188**, 406–415 (2020). https://doi.org/10.1016/j.actamat.2020.02.023. URL https://linkinghub.elsevier.com/retrieve/pii/S1359645420301270

[18] B. Gault, B. Klaes, F.F. Morgado, C. Freysoldt, Y. Li, F. De Geuser, L.T. Stephenson, F. Vurpillot, Reflections on the Spatial Performance of Atom Probe Tomography in the Analysis of Atomic Neighborhoods. Microscopy and Microanalysis pp. 1–11 (2021). https://doi.org/10.1017/S1431927621012952. URL https://www.cambridge.org/core/product/identifier/S1431927621012952/type/journal_article

[19] F. Vurpillot, A. Bostel, E. Cadel, D. Blavette, The spatial resolution of 3D atom probe in the investigation of single-phase materials. Ultramicroscopy **84**(3-4), 213–224 (2000). https://doi.org/10.1016/S0304-3991(00)00035-8. URL https://linkinghub.elsevier.com/retrieve/pii/S0304399100000358

[20] F. Vurpillot, G. Da Costa, A. Menand, D. Blavette, Structural analyses in three-dimensional atom probe: a Fourier transform approach. Journal of Microscopy **203**(3), 295–302 (2001). https://doi.org/10.1046/j.1365-2818.2001.00923.x. URL http://doi.wiley.com/10.1046/j.1365-2818.2001.00923.x

[21] B. Gault, M.P. Moody, F. De Geuser, A. La Fontaine, L.T. Stephenson, D. Haley, S.P. Ringer, Spatial Resolution in Atom Probe Tomography. Microscopy and Microanalysis **16**(1), 99–110 (2010). https://doi.org/10.1017/S1431927609991267. URL https://www.cambridge.org/core/product/identifier/S1431927609991267/type/journal_article

[22] M. Zhu, O. Cojocaru-Mirédin, A.M. Mio, J. Keutgen, M. Küpers, Y. Yu, J.Y. Cho, R. Dronskowski, M. Wuttig, Unique Bond Breaking in Crystalline Phase Change Materials and the Quest for Metavalent Bonding. Advanced Materials (Deerfield Beach, Fla.) **30**(18), e1706,735 (2018). https://doi.org/10.1002/adma.201706735

[23] Y. Yu, M. Cagnoni, O. Cojocaru-Mirédin, M. Wuttig, Chalcogenide Thermoelectrics Empowered by an Unconventional Bonding Mechanism. Advanced Functional Materials **30**(8), 1904,862 (2020). https://doi.org/10.1002/adfm.201904862. URL https://onlinelibrary.wiley.com/doi/abs/10.1002/adfm.201904862

[24] M. Raghuwanshi, O. Cojocaru-Mirédin, M. Wuttig, Investigating Bond Rupture in Resonantly Bonded Solids by Field Evaporation of Carbon Nanotubes. Nano Letters **20**(1), 116–121 (2020). https://doi.org/10.1021/acs.nanolett.9b03435. URL https://doi.org/10.1021/acs.nanolett.9b03435. Publisher: American Chemical Society

[25] M. Herbig, Spatially correlated electron microscopy and atom probe tomography: Current possibilities and future perspectives. Scripta Materialia **148**, 98–105 (2018). https://doi.org/10.1016/j.scriptamat.2017.03.017. URL https://www.sciencedirect.com/science/article/pii/S1359646217301422

[26] L. Mancini, F. Moyon, D. Hernàndez-Maldonado, I. Blum, J. Houard, W. Lefebvre, F. Vurpillot, A. Das, E. Monroy, L. Rigutti, Carrier Localization in GaN/AlN Quantum Dots As Revealed by Three-Dimensional Multimicroscopy. Nano Letters **17**(7), 4261–4269 (2017). https://doi.org/10.1021/acs.nanolett.7b01189. URL https://pubs.acs.org/doi/10.1021/acs.nanolett.7b01189

[27] A. Prakash, J. Guénolé, J. Wang, J. Müller, E. Spiecker, M. Mills, I. Povstugar, P. Choi, D. Raabe, E. Bitzek, Atom probe informed simulations of dislocation–precipitate interactions reveal the importance of local interface curvature. Acta Materialia **92**, 33–45 (2015). https://doi.org/10.1016/j.actamat.2015.03.050. URL https://linkinghub.elsevier.com/retrieve/pii/S1359645415002268

[28] Q.M. Ramasse, C.R. Seabourne, D.M. Kepaptsoglou, R. Zan, U. Bangert, A.J. Scott, Probing the bonding and electronic structure of single atom dopants in graphene with electron energy loss spectroscopy. Nano Letters

13(10), 4989–4995 (2013). https://doi.org/10.1021/nl304187e

[29] P.W. Hawkes, J.C.H. Spence (eds.), *Springer handbook of microscopy*. Springer handbooks (Springer, Cham, 2019). https://doi.org/10.1007/978-3-030-00069-1

[30] B. Deconihout, A. Menand, M. Bouet, J. Sarrau, Performance of an energy compensated time-of-flight mass spectrometer. Surface Science **266**(1-3), 523–528 (1992). https://doi.org/10.1016/0039-6028(92)91070-R. URL https://linkinghub.elsevier.com/retrieve/pii/003960289291070R

[31] M.R. Scheinfein, D.N. Seidman, Time aberrations of uniform fields: An improved reflectron mass spectrometer for an atom-probe field-ion microscope. Review of Scientific Instruments **64**(11), 3126–3131 (1993). https://doi.org/10.1063/1.1144319. URL http://aip.scitation.org/doi/10.1063/1.1144319

[32] A. Cerezo, T.J. Godfrey, S.J. Sijbrandij, G.D.W. Smith, P.J. Warren, Performance of an energy-compensated three-dimensional atom probe. Review of Scientific Instruments **69**(1), 49–58 (1998). https://doi.org/10.1063/1.1148477. URL http://aip.scitation.org/doi/10.1063/1.1148477

[33] E. Bémont, A. Bostel, M. Bouet, G. Da Costa, S. Chambreland, B. Deconihout, K. Hono, Effects of incidence angles of ions on the mass resolution of an energy compensated 3D atom probe. Ultramicroscopy **95**, 231–238 (2003). https://doi.org/10.1016/S0304-3991(02)00321-2. URL http://www.sciencedirect.com/science/article/pii/S0304399102003212

[34] E.W. Müller, S. Krishnaswamy, Energy deficits in pulsed field evaporation and deficit compensated atom-probe designs. Review of Scientific Instruments **45**(9), 1053–1059 (1974). https://doi.org/10.1063/1.1686808. URL http://aip.scitation.org/doi/10.1063/1.1686808

[35] W. Poschenrieder, Multiple—focusing time of flight mass spectrometers Part I. Tofms with equal momentum acceleration. International Journal of Mass Spectrometry and Ion Physics **6**(5-6), 413–426 (1971). https://doi.org/10.1016/0020-7381(71)85019-2. URL https://linkinghub.elsevier.com/retrieve/pii/0020738171850192

[36] W. Poschenrieder, Multiple-focusing time-of-flight mass spectrometers Part II. TOFMS with equal energy acceleration. International Journal of Mass Spectrometry and Ion Physics **9**(4), 357–373 (1972). https://doi.org/10.1016/0020-7381(72)80020-2. URL https://linkinghub.elsevier.com/retrieve/pii/0020738172800202

[37] E.W. Muller, Field Desorption. Physical Review **102**(3), 618–624 (1956). https://doi.org/10.1103/PhysRev.102.618. URL https://link.aps.org/

doi/10.1103/PhysRev.102.618

[38] C. Sánchez, A. Lozovoi, A. Alavi, Field-evaporation from first-principles. Molecular Physics **102**, 1045–1055 (2004). https://doi.org/10.1080/00268970410001727673

[39] C. Freysoldt, A. Mishra, M. Ashton, J. Neugebauer. Density Functional Modelling of Field Evaporation

[40] T. Ono, K. Hirose, First-principles study on field evaporation for silicon atom on Si(001) surface. Journal of Applied Physics **95**(3), 1568–1571 (2004). https://doi.org/10.1063/1.1636258. URL http://aip.scitation.org/doi/10.1063/1.1636258

[41] M. Ashton, A. Mishra, J. Neugebauer, C. Freysoldt, *Ab initio* Description of Bond Breaking in Large Electric Fields. Physical Review Letters **124**(17), 176,801 (2020). https://doi.org/10.1103/PhysRevLett.124.176801. URL https://link.aps.org/doi/10.1103/PhysRevLett.124.176801

[42] T. Ohnuma, First-Principles Calculation of the Evaporation Field and Roll-up Effect of M (M = Fe, Cu, Si, and Mn) on the Fe (001) and Fe Step Structure. Microscopy and Microanalysis: The Official Journal of Microscopy Society of America, Microbeam Analysis Society, Microscopical Society of Canada pp. 1–7 (2021). https://doi.org/10.1017/S1431927621000155

[43] M. Wada, On the thermally activated field evaporation of surface atoms. Journal de Physique Colloques **45**(C9), C9–89–C9–94 (1984). https://doi.org/10.1051/jphyscol:1984916. URL https://hal.archives-ouvertes.fr/jpa-00224394

[44] G.L. Kellogg, Measurement of activation energies for field evaporation of tungsten ions as a function of electric field. Physical Review B **29**(8), 4304–4312 (1984). https://doi.org/10.1103/PhysRevB.29.4304. URL https://link.aps.org/doi/10.1103/PhysRevB.29.4304

[45] N. Ernst, Experimental investigation on field evaporation of singly and doubly charged rhodium. Surface Science **87**(2), 469–482 (1979). https://doi.org/10.1016/0039-6028(79)90542-9. URL https://linkinghub.elsevier.com/retrieve/pii/0039602879905429

[46] F. Vurpillot, in *Atom Probe Tomography*, ed. by W. Lefebvre-Ulrikson, F. Vurpillot, X. Sauvage (Academic Press, 2016), pp. 183–249. https://doi.org/10.1016/B978-0-12-804647-0.00007-3. URL http://www.sciencedirect.com/science/article/pii/B9780128046470000073

[47] L. Zhao, A. Normand, F. Delaroche, B. Ravelo, F. Vurpillot, Pulse shaping optimization for improving atom probe tomography. International Journal of Mass Spectrometry **386**, 47–53 (2015). https://doi.org/10.1016/j.ijms.2015.06.012. URL https://linkinghub.elsevier.com/retrieve/pii/S1387380615001955

[48] D.R. Kingham, The post-ionization of field evaporated ions: A theoretical explanation of multiple charge states. Surface Science **116**(2), 273–301 (1982). https://doi.org/10.1016/0039-6028(82)90434-4. URL https://linkinghub.elsevier.com/retrieve/pii/0039602882904344

[49] L. Rousseau, A. Normand, F.F. Morgado, L. Stephenson, B. Gault, K. Tehrani, F. Vurpillot, Dynamic Effects in Voltage Pulsed Atom Probe. Microscopy and Microanalysis pp. 1–14 (2020). https://doi.org/10.1017/S1431927620024587. URL https://www.cambridge.org/core/product/identifier/S1431927620024587/type/journal_article

[50] X.j. Ge, N.x. Chen, W.q. Zhang, F.w. Zhu, Selective field evaporation in field-ion microscopy for ordered alloys. Journal of Applied Physics **85**(7), 3488–3493 (1999). https://doi.org/10.1063/1.369706. URL http://aip.scitation.org/doi/10.1063/1.369706

[51] Y. Wei, Z. Peng, M. Kühbach, A. Breen, M. Legros, M. Larranaga, F. Mompiou, B. Gault, 3D nanostructural characterisation of grain boundaries in atom probe data utilising machine learning methods. PLOS ONE **14**(11), e0225,041 (2019). https://doi.org/10.1371/journal.pone.0225041. URL https://dx.plos.org/10.1371/journal.pone.0225041

[52] C. Oberdorfer, S.M. Eich, G. Schmitz, A full-scale simulation approach for atom probe tomography. Ultramicroscopy **128**, 55–67 (2013). https://doi.org/10.1016/j.ultramic.2013.01.005. URL https://linkinghub.elsevier.com/retrieve/pii/S0304399113000144

[53] B. Klaes, J. Renaux, R. Lardé, F. Delaroche, F.F. Morgado, L.T. Stephenson, B. Gault, F. Vurpillot, Analytical Three-Dimensional Field Ion Microscopy of an Amorphous Glass FeBSi. Microscopy and Microanalysis pp. 1–9 (2021). https://doi.org/10.1017/S1431927621012629. URL https://www.cambridge.org/core/product/identifier/S1431927621012629/type/journal_article

[54] M.K. Miller, R.G. Forbes, *Atom-Probe Tomography* (Springer US, Boston, MA, 2014). https://doi.org/10.1007/978-1-4899-7430-3. URL http://link.springer.com/10.1007/978-1-4899-7430-3

[55] I. Blum, F. Cuvilly, W. Lefebvre-Ulrikson, in *Atom Probe Tomography* (Elsevier, 2016), pp. 97–121. https://doi.org/10.1016/B978-0-12-804647-0.00004-8. URL https://linkinghub.elsevier.com/

retrieve/pii/B9780128046470000048

[56] B. Gault, X.Y. Cui, M.P. Moody, F. De Geuser, C. Sigli, S.P. Ringer, A. Deschamps, Atom probe microscopy investigation of Mg site occupancy within \(\delta\)' precipitates in an Al–Mg–Li alloy. Scripta Materialia **66**(11), 903–906 (2012). https://doi.org/10.1016/j.scriptamat.2012.02.021. URL https://linkinghub.elsevier.com/retrieve/pii/S1359646212001133

[57] in *https://www.cameca.com* (2020)

[58] E.W. Muller, Das Feldionenmikroskop. Zeitschrift fur Physik **131**(1), 136–142 (1951). https://doi.org/10.1007/BF01329651. URL http://link.springer.com/10.1007/BF01329651

[59] C. Pareige, W. Lefebvre-Ulrikson, F. Vurpillot, X. Sauvage, in *Atom Probe Tomography* (Elsevier, 2016), pp. 123–154. https://doi.org/10.1016/B978-0-12-804647-0.00005-X. URL https://linkinghub.elsevier.com/retrieve/pii/B978012804647000005X

[60] in *https://www.integratedsoft.com/* (2020)

[61] H. Lashgari, J. Cadogan, D. Chu, S. Li, The effect of heat treatment and cyclic loading on nanoindentation behaviour of FeSiB amorphous alloy. Materials & Design **92**, 919–931 (2016). https://doi.org/10.1016/j.matdes.2015.12.136. URL https://linkinghub.elsevier.com/retrieve/pii/S0264127515309965

Supplementary Files

This is a list of supplementary files associated with this preprint. Click to download.

- SupportingInformation6.avi